Available online at www.sciencedirect.com

ScienceDirect

Additive Manufacturing 6 (2015) 53–66

Additive MANUFACTURING

www.elsevier.com/locate/addma

Incremental metal-powder solidification by localized microwave-heating and its potential for additive manufacturing

Eli Jerby [a,*], Yehuda Meir [a], Alon Salzberg [a], Eli Aharoni [a], Ariel Levy [a], Javier Planta Torralba [b], Benjamin Cavallini [b]

[a] *Faculty of Engineering, Tel Aviv University, Ramat Aviv 69978, Israel*
[b] *ASCAMM Prívate Foundation, Av. Universitat Autònoma, 23, 08290 Cerdanyola del Vallès, Spain*

Accepted 16 March 2015
Available online 23 March 2015

Abstract

This paper presents a concept of solidifying small quantities of metal powders in an additive manner, using localized microwave heating (LMH). The experimental results show solidification of metal powders in forms of spheres and rods (of ∼2 mm diameter) and extension of these rods by adding batches of powder and consolidating them locally as building blocks by LMH. A theoretical model applied for the LMH interaction with metal powders attributes a magnetic heating effect also to powders made of non-magnetic metals, due to eddy currents. The experimental observations and numerical results also suggest that micro-plasma discharges between the powder particles initiate their heating process. The additive LMH approach presented here is intended to extend microwave sintering capabilities, mainly known in volumetric molds, also to applications in the framework of rapid prototyping, additive manufacturing, and 3D-printing. The potentials and limitations of the powder solidification by LMH are discussed in this view.

Keywords: Additive manufacturing; 3D printing; Localized microwaves; Sintering; Metal powder

1. Introduction

Microwave applications for material processing, such as ceramic sintering, have been studied extensively (e.g. [1–3] and references therein). Roy et al. [4] discovered that metal powders can also be sintered effectively by microwaves in molds. Microwave sintering processes were demonstrated for metals (e.g. tungsten, copper [5,6]) and metal-oxides (ferrites [7], transparent alumina [8], metallic glass [9]). Susceptors [10] and polymeric binders [11] were found useful in some microwave sintering processes. Microwave heating and sintering processes are applicable for a variety of metal-based materials [12]. Experimental evidences show the capabilities and advantages of microwave sintering of metal-based powders (such as time and energy savings, and improved mechanical properties) compared to conventional techniques.

Microwave-sintering processes are usually performed volumetrically within molds in customized cavities or in microwave applicators, with transverse dimensions comparable to the microwave wavelength employed ($\lambda_0 \simeq 12$ cm at 2.45 GHz). In the industry, however, mold fabrication is suitable for mass manufacturing of large series but it might be wasteful in small quantities. The latter require more versatile techniques, as provided by advanced additive manufacturing (AM) technologies [13].

Beside the major trend of mass production in manufacturing industries, there is also a growing need for custom-made products. Such items, tailored for specific needs, are produced in small quantities or even in single units (as for instance personally adapted prostheses). Similarly, industries in the aerospace, automotive and military sectors are interested as well in custom capable technologies to manufacture unique products with complex geometries. Therefore, rapid prototyping (RP) and AM techniques have been widely studied and developed in the last decade [14]. In these techniques, the fabricated objects are built up layer-by-layer from 3D models programmed by

* Corresponding author. Tel.: +972 36408048.
E-mail address: jerby@eng.tau.ac.il (E. Jerby).

http://dx.doi.org/10.1016/j.addma.2015.03.002
2214-8604/

computer-aided design codes. These processes eliminate tooling and reduce production time and cost. Their performance can be addressed in terms of production volume, complexity and customization of the fabricated product. Such processes are also suitable for low volume production of materials difficult to process, and for the fabrication of complex parts of high aggregate values for automotive and aerospace industries [15]. They also offer a large potential for mass-customization, as for example the fabrication of implants for the biomedical industry [16].

Laser-based sintering processes in optical wavelengths (about $\times 10^5$ shorter than the ~10 cm microwave wavelengths) can be performed locally, without molds, and yet remotely in the far field of the laser beam. Lasers are applicable for AM of metal parts in various schemes [17]. In the selective laser sintering (SLS), the object is created layer-by-layer from powder heated locally by a scanning laser-beam process [18,19]. Lasers are applicable directly for metal powders in techniques also referred to as direct metal laser sintering (DMLS). Such a layer-by-layer AM approach may also be applicable by using microwave energy [20].

Electric-discharge techniques enable rapid heating and eliminate the need for susceptors to reach high temperatures. The spark plasma sintering (SPS) process [21] demonstrates sintering, consolidation and crystal growth by spark plasma systems. Rapid discharge sintering (RDS) [22] employs microwaves in order to excite plasma from gas around the sample. An ultrasonic melting technique [23] is employed for 3D manufacturing of plastic parts from powders.

The proposed utilization of localized microwave heating (LMH) [24,25] enables the incremental solidification of metal powders, similarly to the laser-based SLS technique. Microwave devices could be simpler and smaller, and in some scenarios also more cost-effective than laser-based solutions, hence the motivation proposed to integrate them in RP and AM systems. This approach may lead for instance to a direct metal microwave sintering (DMMS) concept, either as a substitute for the known laser-based DMLS technique or combined with it (in order to benefit from both the laser superior resolution and the microwave effectiveness in larger volumes). In this paper, the processes of incremental metal-powder solidification by LMH is examined. Experimental and theoretical results that demonstrate the fundamental feasibility of the proposed LMH-AM technique are presented accordingly.

2. The localized microwave-heating (LMH) concept

The proposed AM process for metal powders is based on the LMH effect [26,27]. Unlike common volumetric microwave techniques, the LMH applicator intentionally concentrates the microwave-heating energy in the processed materials into regions much smaller than the microwave wavelength. The LMH effect has been demonstrated by the microwave-drill operation [26]. The underlying physical effect that enables its sub-wavelength energy concentration is the induced thermal-runaway instability. The consequent localization effect [28] enables for instance the focusing of 2.45 GHz microwaves into a ~1 mm$^{\emptyset}$ spot within the material (two orders of magnitude smaller than the 122 mm wavelength). The thermal-runaway instability, attributed to the temperature dependence of the material properties, enable a heating rate of >300 K/s in the confined hotspot. This unique capability of the localized microwave heating enables drilling as well as other localized material-processing applications usually performed by lasers [29]. Unlike the remote laser operation, the localized microwave concentration is a near-field effect which requires a close proximity (or even a physical contact) of the microwave applicator and the processed object.

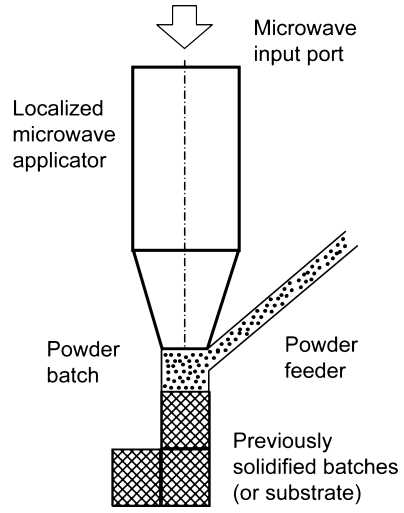

Fig. 1. A conceptual illustration of the incremental powder solidification process using a localized microwave heating (LMH) applicator [24,25].

Localized microwave effects were demonstrated by microwave-drill applicators in various materials, including concrete and glass [30], silicon [31,32], ceramics [33], thermal-barrier coatings [34], and bones [35]. LMH techniques were also studied for the conversion of solid metals to powders by means of plasma ejection from the hotspot induced [36]. This conversion of solid metal to powder can be regarded to some extent as an inverse of the powder solidification technique presented in this paper. LMH was also found useful for effective ignition of pure thermite powders [37]. Microwave generators can also be implemented by advanced solid-state devices, which enable compact, low-cost LMH applicators [38].

The proposed method of stepwise forming of solid bodies from metal powders by means of LMH [24,25] intentionally applies the effect of hotspot formation by thermal-runaway instability. This effect enables local melting of small amounts of powder also in successive steps, hence the extension of a previously sintered substrate in an incremental manner in order to construct a larger structure. The localized microwave applicator is illustrated in Fig. 1. A small batch of powder, positioned by a feeder in front of it, is subjected to LMH interaction. In the stepwise AM process, each batch of powder provides a volumetric pixel (a voxel) which is solidified sequentially by LMH and consolidated, as an additional building block, with the previously constructed structure.

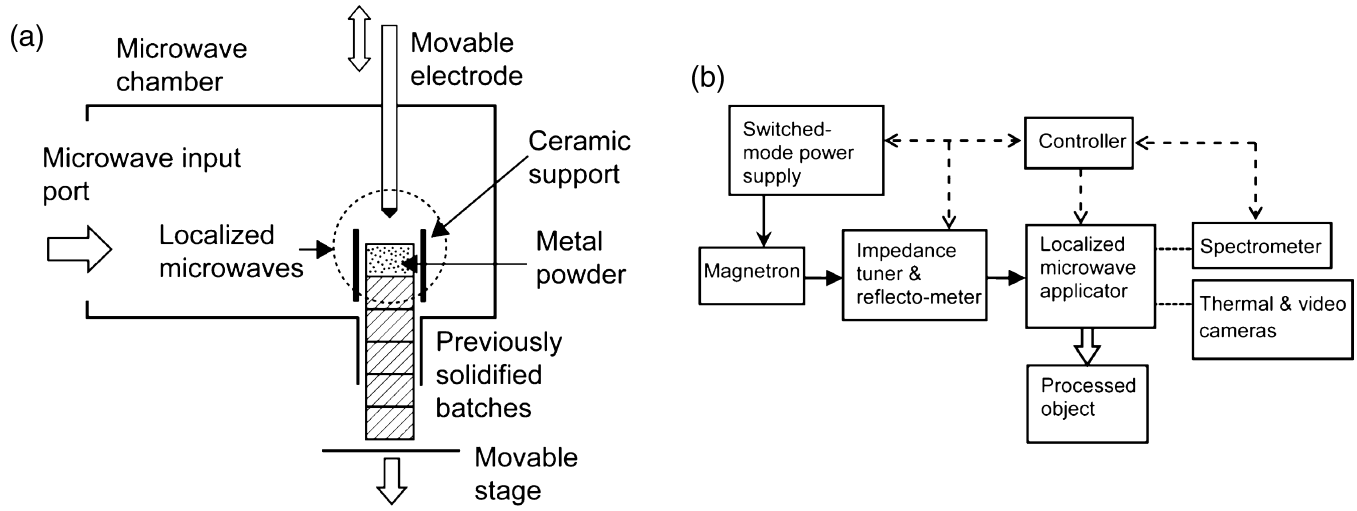

Fig. 2. The experimental setup: (a) An illustration of the LMH applicator used to study the stepwise solidification process in one dimension. The powder batch (typically 1–30 mm^3) was fed and supported by a ceramic tube. (b) The peripheral equipment used in this experimental setup.

3. Experimental setup

A block diagram of the experimental setup used in this study is depicted in Fig. 2a and b. The LMH applicator, used in these experiments to study additive extensions of rods, is illustrated in Fig. 2a. The LMH effect can be enhanced by a movable electrode (as in the microwave-drill interaction [26,28]) which intensifies the electric field in the vicinity of the powder batch. In these experiments, this optional electrode was made of a 1.6 or 2.4 mm diameter tungsten rod. The typical volume range of a single powder batch used as a building block (a voxel) was ~1–30 mm^3. Much larger voxels of ~800 mm^3 were successfully processed as well. The heat generated locally by the thermal-runaway instability enabled the confined microwave solidification process of the metal powder. The experiments presented here mainly utilized bronze-based powder with fine grains (DirectMetal-20, EOS, GmbH) designed for laser sintering of products with good corrosion resistance [39]. The magnetic fixation experiments presented in Section 4.4 were performed with iron powder of a 149 μm grain size (Carlo-Erba, France, >97% assay).

The peripheral components of the experimental setup (Fig. 2b) included a magnetron tube powered by a controlled switched-mode converter (MagDrive-1000, Dipolar, Sweden) which generated a 2.45 GHz frequency in the range of 0–1 kW output power. The microwave reflections from the processed material were detected by a reflecto-meter, and were reduced continuously by an adaptive impedance tuner (Homer, S-Team, Slovak Republic). The magnetron was also protected by an isolator (not shown in Fig. 2b). An optical spectrometer (AvaSpec-3648, Avantes, The Netherlands) and video camera were used for diagnostic purposes. A thermal camera (FLIR-SC300, USA) in the range of 350–1400 K was used to measure the temperature profile evolved. A LabVIEW code controlled the system, and accumulated the experimental data.

The surface morphology of the solidified objects was characterized by an environmental scanning electron microscope (ESEM), Quanta 200FEG (FEI Co., Hillsboro, USA), using secondary electron (SE) and solid-state backscattered electron (BSE) detectors. The elemental content of the material tested was revealed by energy disperse spectroscopy (EDS) analysis with a Si(Li) liquid-nitrogen cooled Oxford INCA X-ray detector. The hardness of the produced objects was measured using a micro-hardness tester (Future-Tech, FM-700e, Japan).

4. Experimental results

The feasibility of the proposed concept was initially studied here by various experiments, specifically aimed at the various stages of solidification and AM of metal powders by LMH. The first experiment was intended to examine the solidification of a small quantity of powder, in order to form the basic building block (to be used as a voxel). The next stage was the solidification of a small batch of powder attached to a previously constructed object in order to study the fundamental additive feature of the proposed technique. The final stage in this set of experiments was aimed to study the solidification of an object extended by successively repeating steps of powder solidification and consolidation. This process was demonstrated here by an AM of rod in 14 steps to a 10 mm length. In addition, a magnetic fixation technique was studied (instead of mechanical supports) in order to hold the powder batch fixed in free space while being melted and consolidated. The results of these experiments and the ex situ analyses of their products demonstrate the LMH relevance for RP and AM applications.

4.1. Solidification of 2 $mm^{Ø}$ spheres

This experiment was conducted using a movable electrode which picked up a batch of powder and locally radiated it by microwaves. The applicator shown in Fig. 2a was excited by a ~0.9 kW microwave power. The movable electrode was lowered to interact with the metal powder surface, and was then elevated to ~10 mm above it. A plasma plum, ejected while the electrode touched the powder surface, enhanced the heating process. The powder attached to the electrode tip was melted locally in a form of a sphere (~2 mm diameter) in free space. It was solidified

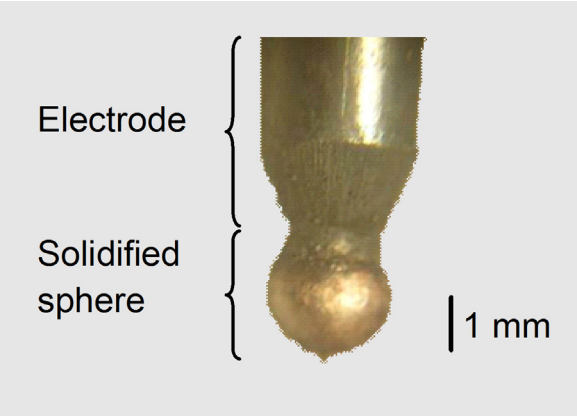

Fig. 3. A single ~2-mm^{Ø} sphere solidified by LMH from bronze-based powder in free space, using a pickup electrode made of tungsten.

when the microwave was turned off, and could be remained then attached to the pickup electrode (as seen in Fig. 3) or be separated from it. This basic process demonstrates the feasibility of single sphere solidification in free space, as an essential capability needed for the construction of more complicated structures.

4.2. AM of ~2-mm^{Ø} rods

Using the experimental setup shown in Fig. 2a and b, a batch of powder positioned by a ceramic tube was exposed to localized microwave radiation directed by a tungsten electrode. During the LMH interaction, a plasma plume was ejected from the metal powder, which was partially molten. The solidified cylindrical block obtained in the first step is shown in Fig. 4a and b. In the next step, another batch of powder was added on top of the previously solidified block, and the process was repeated with all other conditions the same as before. Consequently, the second batch of powder was solidified and consolidated with the previous block. Thus, a solid ~2-mm^{Ø} rod of ~6-mm length, shown in Fig. 4c, was produced in two successive steps.

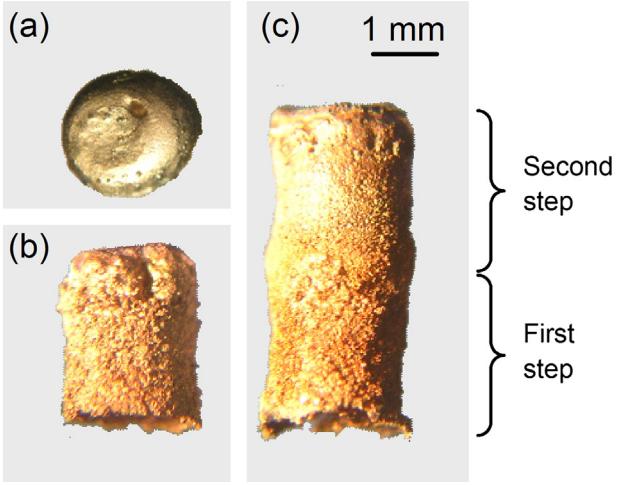

Fig. 4. Upper (a) and side (b) views of a ~2 mm^{Ø}, ~3 mm length rod, solidified from bronze-based powder in the LMH setup shown in Fig. 2a and b. In a successive second step, the rod was additively extended to a ~6-mm length (c).

Fig. 5. An AM of a 2-mm^{Ø} metal rod constructed in 14 consequent steps (repeating the process shown in Fig. 4). The additive stepwise process resulted in a ~10-mm long rod made of solidified increments of bronze-based powder.

Similarly, the extension operation presented above can be repeated sequentially, in any direction. Other experimental runs with more sequential steps demonstrate the formation of longer rods with finer step construction. Fig. 5 shows for instance a solid ~2 mm^{Ø} rod successively constructed in 14 sequential steps to reach a total length of ~10 mm (each incremental step added a solidified voxel of a ~2 mm^3 volume on average). These results demonstrate the LMH capability of incremental solidification, which is essential for the proposed additive technique.

The microwave power absorbed in a single batch (shown in Fig. 4b) and the consequent temperature rise of the whole voxel during a typical step (lasting ~1 s) are shown in Fig. 6. The corresponding microwave power absorbed indicates that the energy absorption within the sintered object was in the order of ~0.1 kJ/mm^3. The consequent heating rate of ~500 K/s is significantly faster than the spontaneous cooling rate of the molten powder after the microwave power was turned off. The spatial thermal image of the voxel and the electrode above it, presented in Fig. 6b, indicate that the whole voxel was heated by the localized microwaves. The measured averaged temperature was lower than the melting temperature of copper in a bulk form (1358 K), due to the diverse powder composition and its partial melting, as described in Section 4.5 (note that the temperature measurements during this LMH-AM process were subjected to some uncertainties due to the rapid heating rates, the relatively small sizes of the samples, and the unknown emissivity of their surfaces. The temperature was estimated therefore by both the black-body radiation emitted from the outer surface during heating, and by the ex-situ observed structural phase-changes which confirmed the lowest temperature estimate in the internal bulk).

The spectral composition of the plasma emitted during the sintering process is shown in Fig. 7a. The spectral content was examined using the microwave-induced breakdown-spectroscopy (MIBS) technique [40]. Copper lines were clearly identified according to the main powder's composition, in addition to impurities of sodium and possibly potassium. A spectrum achieved by a longer exposure to the plasma emission, including intensity calibration in this wavelength range, is presented in Fig. 7b. Copper lines were revealed again with possible impurities of potassium or sodium. The dashed curve shows a fitting of the black-body radiation in the 0.45–0.8 μm range with a temperature of 2490 K, providing an estimate for the gas temperature inside the plasma [41]. Its accuracy is limited though since it only includes part of the radiating spectrum (according to Wien's displacement law) whereas the peak of the temperature is above the detected range. This temperature is higher than the molten powder temperature revealed in Fig. 6b. Plasma emitted

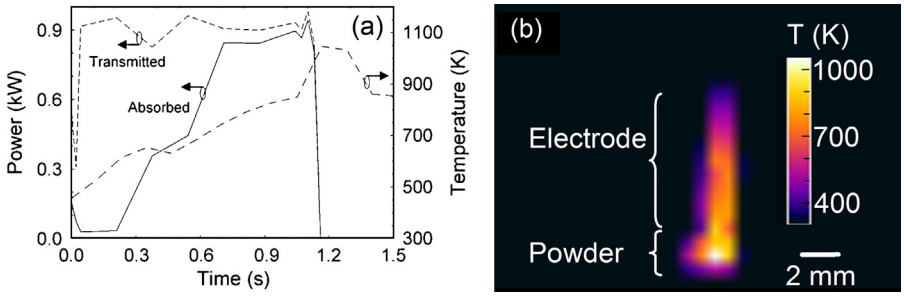

Fig. 6. (a) The transmitted microwave power and its effective portion absorbed by a single powder batch (as shown in Fig. 4b), and the temperature evolved in a typical solidification step during ~1 s. (b) A thermal image of the temperature profile evolved on the powder surface.

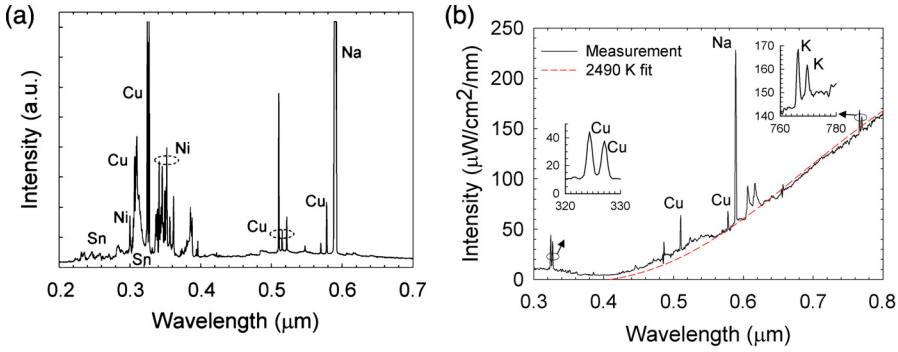

Fig. 7. Optical spectra of plasma discharges observed within the powder: (a) the original spectrum reveals mostly copper lines with possible nickel and tin. (b) The intensity calibrated spectrum shows the gas temperature from the continuum emission fit (dashed line) to black-body radiation.

from the molten voxel may yield a buoyant fireball [42] (which has to be suppressed in practical systems).

An accumulation of 68 experimental runs of the basic solidification step (as in Fig. 4b) is presented in Fig. 8. This chart shows the duration of the LMH process, and the number of runs vs. the transmitted microwave power. The bar chart presents the number of successful operations (resulted in solidification) and the number of failures in each power range, whereas the dots show the actual process duration vs. power. On average, the successful cases are characterized by a power level of 0.5–0.7 kW and duration of ~1 s. Therefore, the corresponding energy density consumed in these experiments was also in the order of ~0.1 kJ/mm^3 on average. This relatively low energy consumption (compared to larger batches) is attributed to the small amount of powder, the directed electrode, and the inner plasma effect. These experiments demonstrate the feasibility of LMH sintering for AM by solidifying powder batch to previously sintered blocks in a stepwise manner.

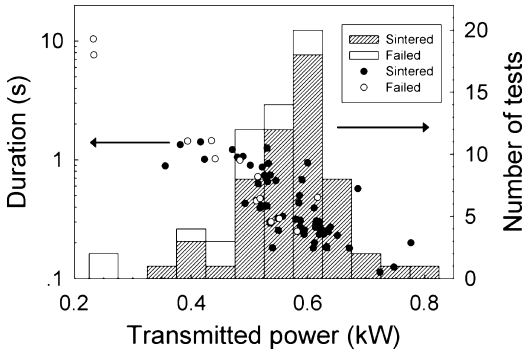

Fig. 8. Results accumulated in 68 experimental runs of single LMH solidification steps, as in Fig. 4b. A batch of bronze-based powder was solidified in each step to a form of a ~2 mm^{Ø}, ~3 mm long rod. The dots show the LMH process duration as a function of the microwave power, whereas the bar chart presents the success and failure rates in these conditions.

4.3. AM of ~10-mm^{Ø} rods

The LMH technique is also applicable for the solidification of relatively large batches of metal powders, and their AM. For instance, Fig. 9a and b show a ~10 mm^{Ø} rod additively constructed in two steps, each add a ~10 mm length to the rod. These batches were larger than the above but yet smaller than the 12 cm microwave wavelength. The LMH process for a single batch of this size lasted ~4 min in 0.9 kW microwave power input. The powder batch was confined by a 10 mm^{Ø} borosilicate glass tube. The electrode was applied as shown in Fig. 2a. The radiated powder glowed in yellow-orange colors, as shown in Fig. 9a, with some plasma ejected (extinguished by air pressure in order to ensure the efficient absorption of the microwave energy by the metal powder rather than the plasma). The rod solidified in two steps is shown in Fig. 9b (after a slight turning in order to remove glass debris and reveal the full solid body). It is noted that the interface between adjacent stages cannot be identified by eye (as in the sample shown in Fig. 9b). This post-processing treatment improved the surface smoothness, as done in other additive techniques such as fused deposition modeling (FDM) [43]. This experiment, performed repeatedly with similar results, demonstrates the feasibility of solidifying and consolidating relatively large batches of metal powder with

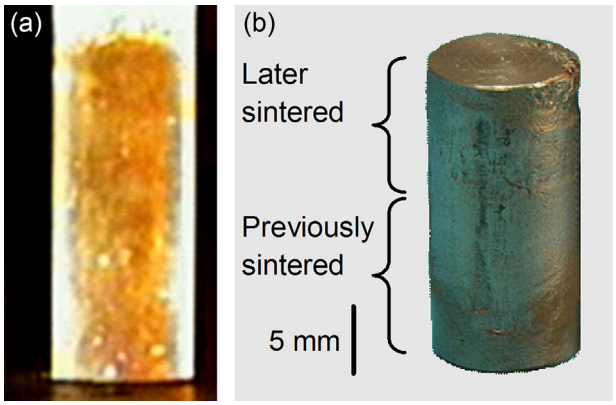

Fig. 9. (a) Glow observed during metal-powder solidification by microwave irradiation in a glass tube. (b) AM of a 10 $mm^{\emptyset}$ rod in two stages. The previously sintered rod is extended by adding another batch of powder bound by the glass tube. The microwave radiation solidifies the additional batch and consolidates as an extended solid rod in each step (the product was slightly machined after the LMH process in order to improve its surface smoothness).

previously sintered blocks. In the AM context, it demonstrates the LMH diversity in construction of 3-D structures by stepwise solidification of metal-powder batches in various sizes.

4.4. Magnetic confinement of metal powders

A contact-less means to hold the powder batch during the LMH interaction, instead of ceramic or glass tubes used above, could be provided by a magnetic fixation of metallic powders which possess magnetic properties (e.g. iron-based powders) [44]. The fixation ("freezing") mechanism illustrated in Fig. 10 may include the following stages: (a) Feeding the powder batch by a mechanical support in any desired shape and direction, (b) applying a static magnetic field to fix the powder in this shape, (c) removing the mechanical support and applying microwave radiation directly to the powder batch fixed by the static magnetic field, and (d) feeding another batch and repeating the process in a stepwise manner.

External magnetic field applied to magnetic powder heap imposes a unique shape of the particle arrangement either in a static or dynamic flow powder. The inter-particle interaction involved depends on the angle β between the magnetic field and the vector connecting the two particles. The force between the powder particles can be attractive or repulsive (for $|\beta| < 55^\circ$ or $55^\circ < |\beta| < 90^\circ$, respectively) [45]. At its maximal value, when the particles are positioned directly one above each other ($\beta = 0$) the magnetic attraction force is given by $F_M = M\sigma_M \nabla \mathbf{B}_\perp$, where M and σ_M are the powder's mass and magnetic moment per mass, respectively, and $\mathbf{B}$ is the magnetic flux-density vector. The gravitation force applied in addition is given by $F_G = Mg$, where $g = 9.8\ m/s^2$ is the gravitational acceleration and $\sigma_M = 218\ Am^2/kg$ for iron [46]. By a comparison of these opposed forces, the magnetic field gradient required to hold the powder shall attain

$$\nabla \mathbf{B}_\perp > \frac{\sigma_M}{g}. \quad (1)$$

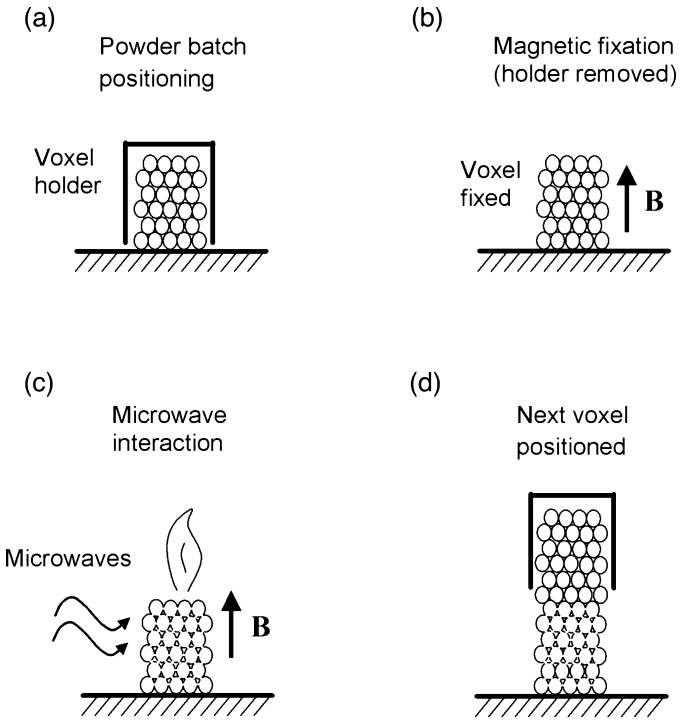

Fig. 10. Contact-less fixation of a magnetic powder batch for stepwise LMH consolidation. (a) The powder batch was positioned by a holder. (b) A static magnetic field was applied to hold the powder fixed. (c) The mechanical support was removed, and the microwave radiation was applied directly to the powder batch fixed by the magnetic field. (d) Another batch of powder was positioned on the previously solidified structure, and the process was repeated in a stepwise manner.

In the present experimental conditions, the threshold value resulted from Eq. (1) is 4.5 G/cm for the magnetic-field gradient. In a larger value, the particles would spontaneously aggregate to a cluster (as is also observed in water [47]). A static magnetic-field distribution as required within the powder batch in order to hold it fixed could be synthesized by an array configuration of magnets [48].

The feasibility of magnetic confinement was examined therefore in order to alleviate the need for a mechanical support for the powder batch during its solidification and consolidation by the localized microwaves. An iron powder was used instead of the bronze-based powder, due to the high magnetic permeability of the iron. This experiment was performed using a permanent magnet which induced a vertical magnetic field of ~0.1 kG and a gradient of ~20 G/cm in the interaction region (well above the threshold dictated by Eq. (1)). After the powder batch was positioned by the ceramic support, as in previous experiments, the static magnetic field was applied. The powder batch preserved therefore its original voxel shape. The mechanical support was then removed, and the microwave power was applied to solidify the powder batch in free space. As presented in Fig. 11a–c, this process can be performed repeatedly in order to fabricate larger objects additively. A single ~3 $mm^{\emptyset}$ bar of ~8 mm length was solidified in five steps. Such bars can be further extended, also horizontally, along the magnetic field lines, in order to construct 3-D structures with no further supports (since the magnetic attraction dominates the gravity force effect on the metal

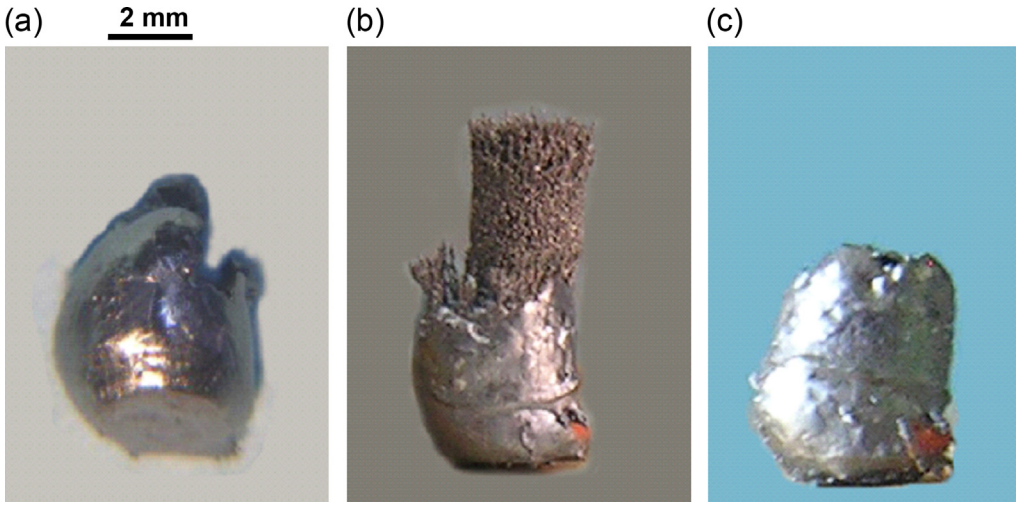

Fig. 11. Magnetic confinement of iron powder in a 2-step experiment. (a) The first voxel solidified. (b) Extension of second powder batch by magnetic field holding on the top of the voxel. (c) The solidification of the added batch.

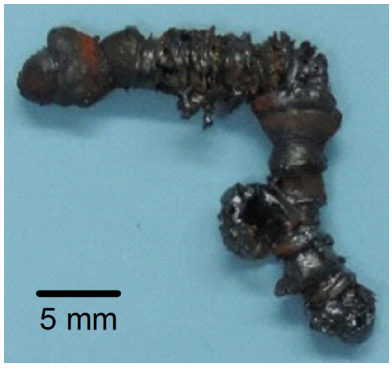

Fig. 12. A preliminary demonstration of LMH stepwise construction (also horizontally) using a magnetic confinement.

powder). The preliminary result shown in Fig. 12 demonstrates the magnetic confinement feasibility for LMH-AM processes (though the surface quality obtained is not yet satisfying).

The magnetic confinement is applicable to materials having sufficiently large magnetic moment in order to conduct the magnetic field along the constructed object, and to attract the particles. Similar results were achieved using a commercial alloy steel powder (DirectSteel-20, EOS, GmbH). Since the construction direction does not necessarily have to be vertical, curved objects in two or three dimensions can be fabricated by varying the magnetic field orientation with respect to the constructed object [44]. This method can also be applicable to materials possessing low magnetic permeability in a bulk form but can be aligned by a magnetic field in a powder form. This magnetic confinement approach may provide simpler and faster supports than mechanical means, and it may enable the construction of more complicated structures.

4.5. Mechanical and structural characterization of LMH-AM products

The various bronze-powder objects produced in the experiments above, of stepwise microwave solidification, were analyzed by mechanical and structural diagnostics in order to characterize the products obtained in this experimental LMH-AM technique. The product's density (mass to volume ratio) was estimated using Archimedes' law (by weighting and then sinking the object in water to find its volume). The resulted density obtained was $7.3 \pm 1\ g/cm^3$. Conventional sintering of similar samples conducted in a furnace at 1200 °C for 20 min yielded a similar density to the LMH result. A laser sintering of the same powder produces however a slightly lower density of $6.26\ g/cm^3$ [49] (note that according to the powder's manufacturer specification, laser sintering may yield 6.3 and $7.6\ g/cm^3$ inner and outer densities, respectively [39]). Compared also to solid copper density ($8.96\ g/cm^3$), the compactness obtained indicates a reasonably low porosity.

The hardness of the stepwise solidified objects, analyzed by a micro-hardness tester at 10 g for 16 s, resulted in 208 ± 42 HV for the voxel bulk regions, and for the interface between voxels as well (verified in 20 measurements). This hardness obtained by LMH is comparable to that obtained by laser sintering [50] and is considerably higher than the 115 HV value specified for this powder in laser sintering [39]. In general, the hardness depends on the remaining porosity and on the cooling rate after sintering [51], both are controllable to some extent in the LMH process.

The inner structure of objects solidified in two steps, as presented in Fig. 4c, were observed along their axial cross-section. For this purpose, the cylindrical object was fixed in epoxy and cut along its axis. Its cross-section plane was polished to a mirror-like surface roughness (0.05 μm) and etched by a solution of $FeCl_3$(25 g) + HCl (25 ml) + H_2O (100 ml) for the microstructure analysis. The SE and BSE micrographs of the solidified voxel bulk are shown in Fig. 13a and b, respectively. The bulk shown in Fig. 13a reveals dendrite structure with a typical width of ~2.5 μm. This structure, enlarged in Fig. 13b, shows dendrites with no inclusions or other defects. The interface region between the two solidification steps is shown in Fig. 13c and d, by SE and BSE images, respectively. The interface region in Fig. 13c shows more porosity than the bulk (Fig. 13a), and its microstructure shown in Fig. 13d is composed by grain structure

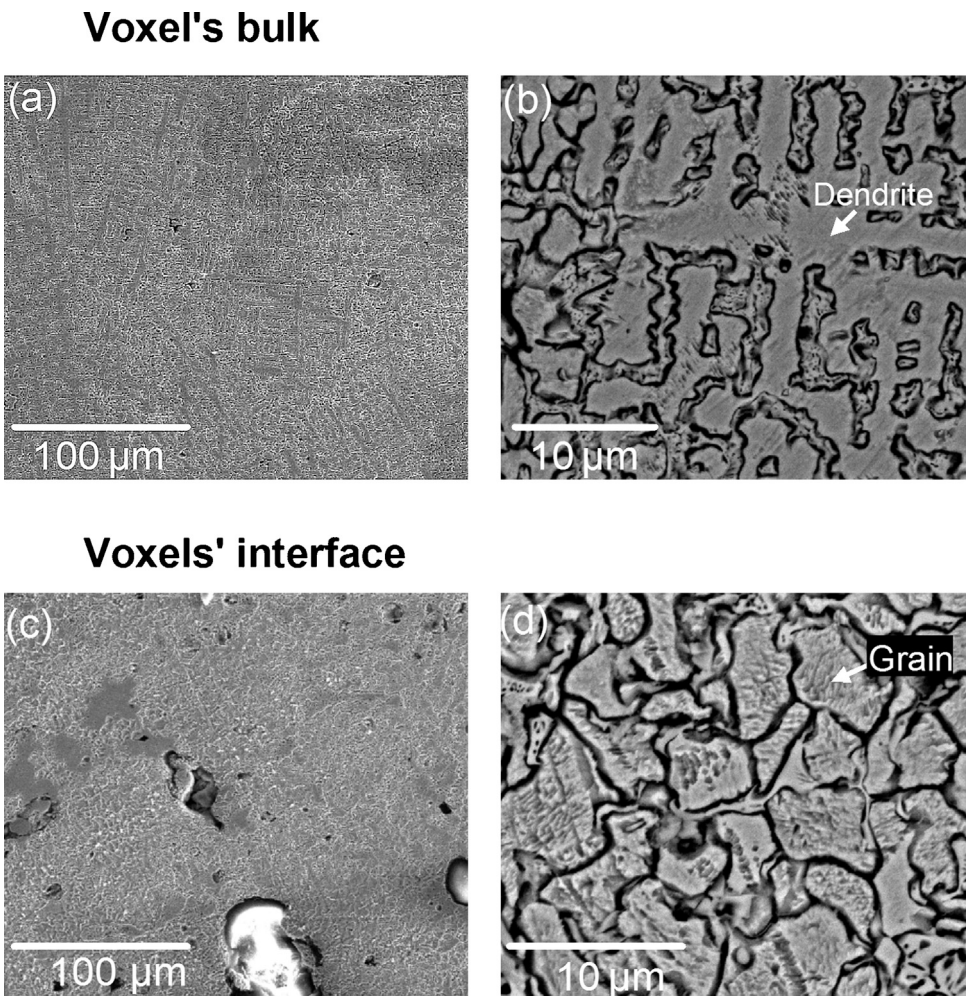

Fig. 13. The bulk micrograph (a) within the solidified voxel and (b) its enlarged dendrite structure. (c) The porous interface between two adjacent voxels and (d) its enlarged grain structure.

with random nucleated grain size of ∼5 μm. Micrographs of larger samples as in Fig. 9 also show a ternary structure with homogeneous morphology and distribution, as well as dendrite structures with thin and uniform morphologies [25].

The powder particles arrangement in a solidified sphere, as in Fig. 3, is seen in the periodical structure obtained by the SE image of the sphere's surface and by its EDS analysis. The selective melting mechanism of the powder content was evidenced by the elemental mapping presented in Fig. 14. The BSE image in Fig. 14a reveals several elements due to the contrast between the powder grains and the matrix between. The EDS analysis at the surface reveals the spatial distributions of copper, phosphorous and tin, in Fig. 14b–d, respectively. The elements with the high melting-temperature in the powder, such as Cu and Ni, are found within the dendrite structure as well as in the grain structure shown in Fig. 13b and d, respectively. While the copper particles are denser at the grains origin, the phosphorous and tin are more evidenced at the solidified liquid phase between the grains. The lower melting-temperature components, including CuSn and CuP, are revealed in the inter-dendrite phase within the dendrites structure in Fig. 13b and in the matrix between the grains shown in Figs. 13d and 14. The particles with the lower melting temperature are expected to firstly melt hence filling the gaps between the pure copper particles, similarly to the distribution observed inside the product. The partial melting contributes to the rearrangement of the particles in the packed form shown in Fig. 14 (Left). The capillary force induced between the solid particles in the wet environment pulls the particles by a liquid bridge meniscus, hence forming more robust structure, as studied numerically by [52]. The addition of Sn and P compounds to the powder is done in order to lower the temperature of the binding elements in the powder, and to improve the mechanical properties of the sintered object in DMLS [53], as also observed by DMMS.

5. Theoretical considerations of LMH mechanisms

Computational models for temperature and energy distributions during AM processes (such as in laser-based system [54]) are essential in order to design and optimize these processes [55]. Here, the initial phase of the LMH process in metal powders is studied. The configuration illustrated for instance in Fig. 1 involves electromagnetic (EM) and thermal processes, which are coupled by the temperature dependencies of the

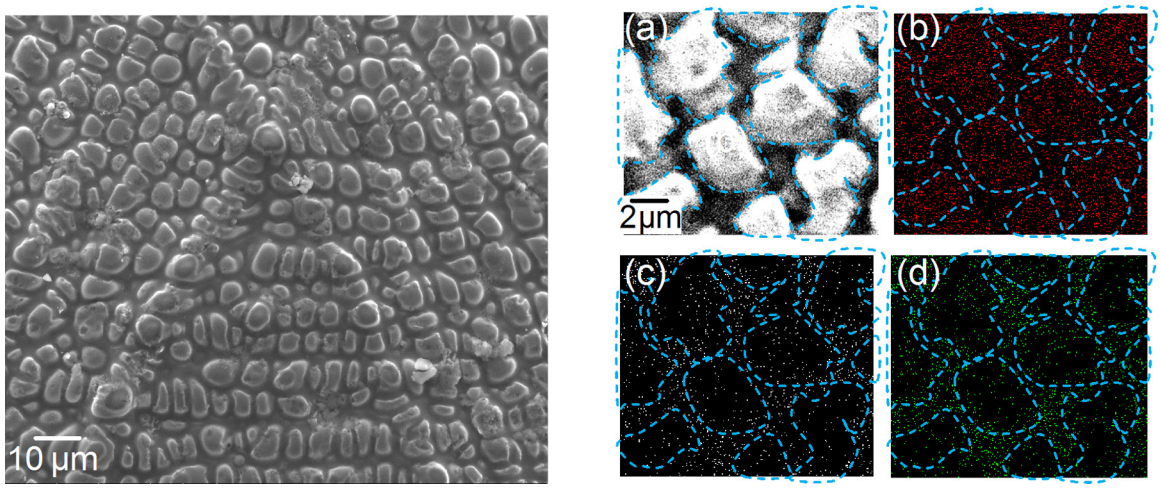

Fig. 14. Left: An SE image of the surface morphology of the solidified sphere as shown in Fig. 3. Right: Element mapping by EDS analysis of the surface shown in the BSE image (a), and its spatial distributions of copper (b), phosphor (c), and tin (d).

material properties. Following the LMH theoretical analysis in solids [28], the coupled microwave-heating model combines here the EM-wave equation and the heat equation in a variable inhomogeneous medium. The latter in this case is the metal powder, which locally varies its properties while being heated.

5.1. The LMH model

The coupled EM and heat equations are presented here in a two-time-scale approach as follows

$$\nabla \times (\mu_r^{-1} \nabla \times \tilde{\mathbf{E}}) - \left[\varepsilon_r' - j\left(\varepsilon_r'' + \frac{\sigma_e}{\omega\varepsilon_0}\right)\right] k_0^2 \tilde{\mathbf{E}} = 0, \tag{2}$$

$$\rho C_p \frac{\partial T}{\partial t} - \nabla \cdot (k_{th} \nabla T) = Q, \tag{3}$$

where $\tilde{\mathbf{E}}$ is the electric vector component of the EM wave in the frequency domain, ω is the angular frequency and $k_0 = \omega\sqrt{\varepsilon_0\mu_0}$ is the corresponding wave number in vacuum, and ε_0 and μ_0 are the vacuum permittivity and permeability, respectively. The metal powder is represented in Eq. (2) by the complex relative values of $\mu_r = \mu_r' - j\mu_r''$ and $\varepsilon_r = \varepsilon_r' - j\varepsilon_r''$, the magnetic permeability and dielectric permittivity, respectively, and by σ_e, the electric conductivity. In the heat equation (3), ρ is the local density of the powder, C_p and k_{th} are its heat capacity and thermal conductivity, respectively, T is the varying temperature profile, and Q is the absorbed power density.

The distinction between the typical time scales of the EM wave propagation and the much slower thermal evolution (in the orders of ~1 ns and >1 ms, respectively) enables one to apply the *two-time scale* approximation. A heuristic indication for the validity of this approximation is provided by the condition $\rho C_p d_{hs}^2 / k_{th} \gg \tau$, where d_{hs} is the hotspot width and $\tau = 2\pi/\omega$ is the EM-wave period. Furthermore, the operating EM spectral bandwidth is sufficiently narrow to neglect the frequency dependence of the permeability and permittivity in the EM time scale. Therefore, the EM wave equation (2) is solved in the frequency domain, while the heat equation (3) is presented in the slowly varying time domain. The EM and heat equations (2) and (3) are locally coupled together by the Q factor, including the ohmic, dielectric, and magnetic heating mechanisms,

$$Q = Q_{ohm} + Q_{diel} + Q_{mag} = \frac{1}{2}\sigma_e(T)|\tilde{\mathbf{E}}|^2 + \frac{1}{2}\omega\varepsilon_0\varepsilon_r''(T)|\tilde{\mathbf{E}}|^2 + \frac{1}{2}\omega\mu_0\mu_r''(T)|\tilde{\mathbf{E}}|^2, \tag{4}$$

and also by the consequent variation of the material's temperature-dependent parameters, $k_{th}(T)$, $\rho(T)$, $C_p(T)$, $\sigma_e(T)$, $\varepsilon_r(T)$ and $\mu_r(T)$. As the temperature rises, the spatial variations in these parameters modify the EM wave propagation pattern within the material, hence enabling the self-focusing effect which characterizes the thermal-runaway process. The coupled EM-heat model above does not include electric discharges or plasma effects which may occur among the metal spheres, and between the powder and the electrode as well.

5.2. Powders' parameters

The solution of the coupled EM-thermal equations (2)–(4), simulating the temporal and spatial evolution of the temperature profile within the powder irradiated by LMH, requires data of the powder parameters and their dependence on the temperature. These parameters differ from those of the bulk material, and depend also on the geometry of the powder particles. For instance, a non-magnetic metal, characterized by $\mu_r = 1$ in a bulk form, may exhibit magnetic properties in a powder state due to the eddy currents induced in the metal micro-particles. Furthermore, the powder may introduce also magnetic heating, represented by the imaginary part of the relative permeability ($\mu_r'' > 0$). This effect is enabled by the electric isolation between the metal particles, caused by their thin dielectric coating due to oxidation, hence the contact resistance between powder particles is assumed to be infinitesimally large in this simulation (this effect is more significant in DC sintering mechanisms and SPS [56]). The electric insulation effect, which enables the

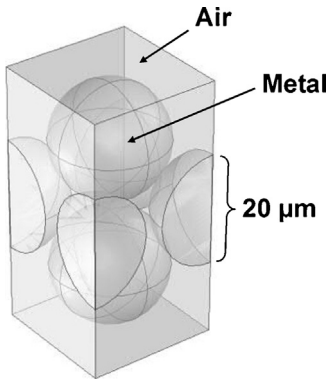

Fig. 15. The powder model as a perfect periodic body-centered cubic (BCC) lattice of isolated metallic spheres.

microwave propagations into the composite, has been investigated in several studies [57–61].

The temperature-dependent parameters of the metal powder (in their effective macroscopic appearance at microwave frequencies) were found here by a model in which the powder particles were represented as a cluster of metallic spheres (20 $\mu m^{\emptyset}$) organized in a periodic body centered cubic (BCC) lattice, as illustrated in Fig. 15. The spheres are isolated by a gap of a few nanometers (due to their outer oxidation layer [60]). The macroscopic parameters were found using the effective-medium approximation (EMA) method [61]. The model was extended here to reconstruct the temperature dependencies of the powder magnetic permeability and of the thermal properties. These include the magnetic heating due to eddy currents evolved within the particles, which may play a major roll also in fine grained metal powders made of non-magnetic metals [4,62]. The magnetic heating mechanism may strengthen the EM-energy coupling to the powder, hence accelerating the localized microwave heating effect before sintering (note that the powder's magnetic properties disappear after its merging to a solidified form).

The results presented in Fig. 16a show the diamagnetic property of the metal powder ($\mu_r' < 1$, in accordance with [60]) and the magnetic losses ($\mu_r'' > 0$), both increase with temperature hence supporting the thermal runaway instability. The effective permittivity of the powder is $\varepsilon_r = 11.2$ with negligible dielectric loss and no temperature dependence. Similarly, the powder's thermal conductivity and capacity were derived from the bulk metal's properties. The thermal conductivity was derived by simulating the temperature gradient generated by a steady-state heating of a thin layer of copper powder, with boundary conditions of a constant temperature on one surface and a constant heat flux on the other one. Its heat capacity was simulated by a uniform heating source within isolating boundary conditions. The thermal properties derived, shown in Fig. 16b, have a tendency to increase with temperature (which suppresses the thermal runaway effect). Therefore, short microwave bursts might be preferred in this case in order to reduce the thermal spread. This reconstruction model is not valid at high temperatures near the material's melting point, in which softening, deformation and necking effects take place.

5.3. LMH simulation results

The simulation results of the coupled EM-thermal model with the powder parameters calculated above are presented in Fig. 17a and b, for 0.9 kW microwave input power. The temperature evolution in time is shown in the validity range of the model up to ~900 K. The resulted heating rate is ~500 K/s at 0.9 kW, and ~200 K/s at 0.6 kW. Consequently, the final hotspot width is narrower in the faster heating process, which is more localized.

The temperature profile reveals the dominance of the magnetic heating effect in this case, since the hotspot surrounds the electrode as a toroid (unlike the microwave-drill effect in dielectric materials [28] in which the hotspot is evolved spherically in front of the electrode). The hotspot width, calculated from the full-width half-maximum (FWHM) of the temperature profile, is in the order of ~2 mm as presented in the inset in Fig. 17b for the case of a dominant magnetic heating. Fig. 17b also shows the effect of the microwave power on the hotspot width at 800 K, and the time required reaching 800 K, in the range of 0.3–0.9 kW (typical to low-cost magnetrons). It is evident from Fig. 17b that the energy range of higher microwave power for shorter durations is preferable for the stepwise sintering process in the aspects of resolution and efficiency. The hotspot size obtained by the simulation (~2 mm) is comparable to the experimental results (e.g. Fig. 3) hence it validates the expected resolution of metal-powder sintering by LMH in AM processes.

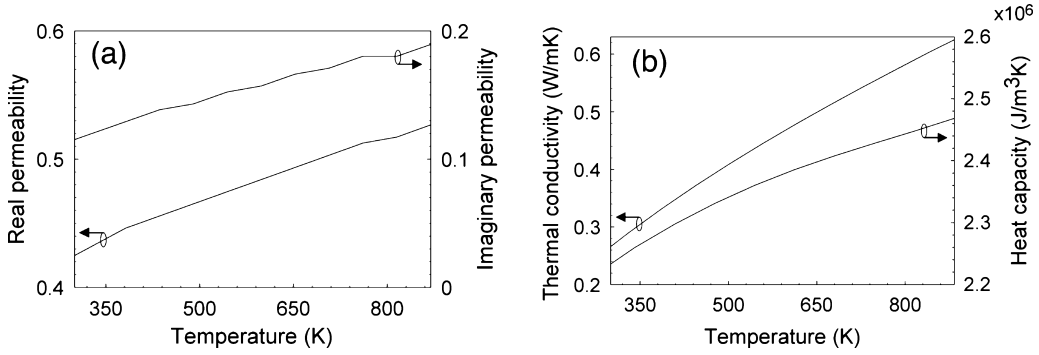

Fig. 16. The temperature dependencies of the powder's permeability (a), and of its thermal conductivity and heat capacity (b), extracted from the theoretical model.

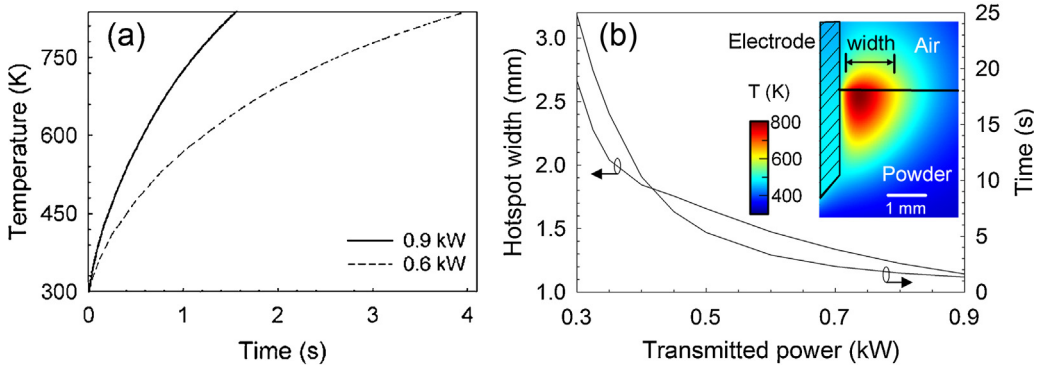

Fig. 17. Simulation results of the hotspot evolved by magnetic heating in metal powder irradiated locally by an immersed electrode in 0.6 kW and 0.9 kW power levels: (a) The maximal hotspot temperature evolved. (b) The hotspot width and required time to reach 800 K vs. the microwave-power applied. The inset shows the temperature profile around the electrode up to 800 K at 0.9 kW and the hotspot width.

The magnetic LMH was demonstrated experimentally by applying the microwave power by an open-end coaxial applicator to copper powder (DirectMetal-20). For the sake of comparison, this experiment employed a relatively low microwave power input (∼0.1 kW) in order to slow down the heating process to a rate enabling real-time detection and comparison with theory [38]. The center electrode of the applicator was inserted to a 1 mm depth into the copper powder. Both the low power applied and the electrode insertion prevent plasma breakdown hence enabling a comparison between experiment and theory of the sole magnetic LMH effect which dominated in this case. The HAZ temperature measured by the thermal camera is shown in Fig. 18a with the theoretical prediction of the model in these conditions. In this case, the magnetic-LMH effect was not characterized by a thermal-runaway instability (as the dielectric LMH) since the temperature tends to stabilize at ∼700 K. The inset in Fig. 18b shows a thermal image of the temperature distribution on the powder outer surface (with no correction for the unknown outer surface emissivity). Its FWHM evolution during the heating process is shown in Fig. 18b. The >2 mm width hotspot was wider than the voxel achieved during the stepwise solidification experiments, because of the relatively low power applied in this benchmark run (note the dependence of the hotspot width on the power in Fig. 17b).

5.4. Micro-plasma effect

Plasma effects may play a significant role in the localized microwave sintering process, in addition to the dielectric and magnetic LMH effects, as observed in the various experimental schemes presented above.

The electric field distribution in front of the electrode, calculated by the EM model at room temperature, is shown in Fig. 19a. The electric field intensity ($|\tilde{\mathbf{E}}|$) enables to compare the fields in the air gap and within the powder, whereas the latter is presented in macroscopic (averaged) values. While these macroscopic fields do not exceed the breakdown threshold, a more detailed analysis in the microscopic level shows that the electric field evolved in the gaps between the powder particles is significantly higher. Fig. 19b shows the field distribution among the powder particles in the BCC arrangement of Fig. 15. The microscopic field is significantly intensified to about twice the maximal electric field shown in Fig. 19a in the macroscopic level.

These results show that the actual electric field, intensified significantly by the particles geometry, satisfies the breakdown condition in the gaps between the powder particles (and yet not in the air gap between the electrode and the powder). The microscopic discharge (as in the DC conditions studied by [63]) may lead to vaporization of the particle surface and to rapid

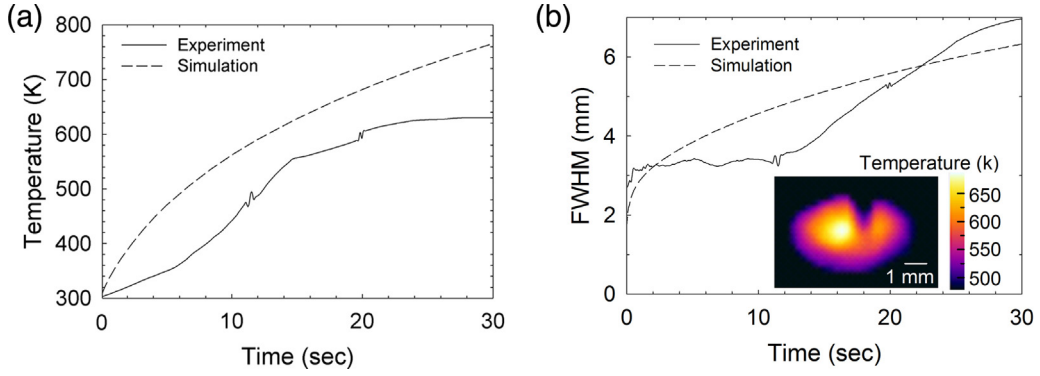

Fig. 18. Experimental and theoretical demonstrations of the initial LMH in metal powder, in a relatively low power of ∼0.1 kW input for the sake of comparison: (a) The hotspot temperature evolution on the powder surface, and (b) the hotspot width. The inset shows the temperature distribution around the electrode on the powder surface, whereas the electrode is inserted 1 mm inside.

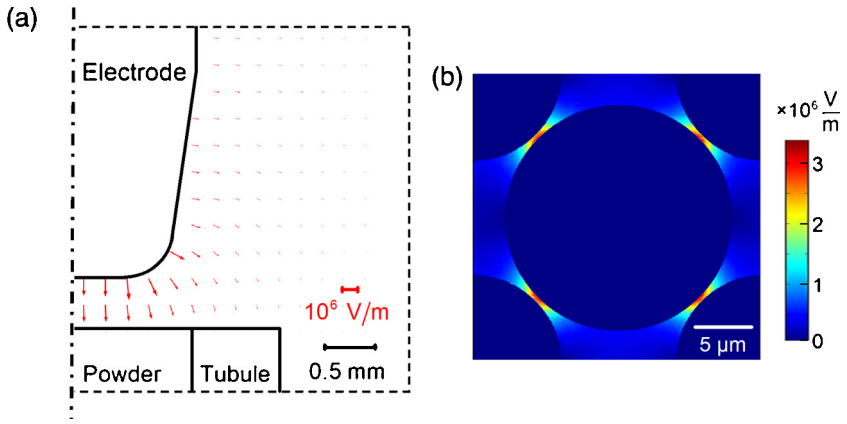

Fig. 19. (a) The electric field distribution ($\tilde{\mathbf{E}}$) in the gap between the electrode and the powder. (b) The actual electric field in the microscopic gaps between adjacent powder particles, exceeding the electrical breakdown threshold in air.

temperature rise within the powder (as in electric-field sintering [56] and microscopic sparking in copper powders [64]). This plasma effect may accelerate as well the LMH process in the dielectric and magnetic mechanisms presented above, as are also observed here experimentally. Further studies are yet needed in this respect in order to incorporate the micro-plasma effect self-consistently into the localized microwave-heating model (2–4).

6. Discussion and conclusion

This work studies incremental sintering processes implemented by LMH, in the context of RP and AM applications. The experimental and theoretical studies presented above demonstrate the feasibility of constructing metal objects from powders by LMH in an additive stepwise manner. The experimental results demonstrate metal-powder solidification in forms of ~2 $mm^{Ø}$ spheres and 2–10 $mm^{Ø}$ rods, as shown for instance in Figs. 3–5 and 9, respectively. This study also demonstrates the feasibility of an incremental extension of sintered bodies in a successive manner, by adding small amounts of powder subjected to LMH. In this stepwise technique, the added powder batch is partially melted by the LMH and by the plasma evolved hence the solidified batch is attached as a building block to the underlying structure.

The theoretical analysis of the initial LMH process in metal powders reveals the dominance of the magnetic over the dielectric LMH mechanism, even in powders made of non-magnetic metals (e.g. copper). However, it also suggests that electric discharges may evolve among the particles and accelerate the microwave heating of metal powders. The model confirms the spatial resolution of the localized microwave sintering process, in the >1 mm range, as is also experimentally observed. Both the experimental observations and the theoretical analyses indicate the potential significance of micro-plasma effects (similarly to SPS and related effects [21,63,64]) as means to intensify the LMH effect within the powder.

The powder assembly was done in these experiments by ceramic feeders and supports, or by static magnetic fields. The latter enable contact-less fixation of magnetic powders and construction of an object in any orientation. For a given microwave energy, the LMH based solidification process is more effective as the microwave pulsed power is higher (in the range of 0.1–1.0 kW) and its duration is shorter accordingly. Microwave processing of metal powders also exhibits a selectivity feature, between the powder and bulk states. While metal in powder form tends to absorb microwave energy (which leads eventually to its melting and solidification), the bulk form of the same metal reflects the microwaves. This natural selectivity may improve the effectiveness of the LMH applied to metal powders in the AM process, compared to other materials.

The material analyses performed on the products obtained by LMH reveal solidified structures with density and hardness better than achieved by laser-based processes with the same powder. The micro morphology shows the partial melting of the powder ingredients, as expected.

The results presented in this paper demonstrate the feasibility of the basic additive operations required for the stepwise construction, as well as the principle feasibility of this concept for AM of more complicated structures. The heating rate achieved (~500 K/s at 0.9 kW) indicates the ability to apply LMH effectively in AM processes. The results presented here provide a basis for various implementations in 3-D printing, RP and AM applications.

In view of the >1-mm resolution achieved in this initial experimental study, and the consequent roughness obtained, the proposed LMH technique could be effectively used as a low-cost means for AM of relatively rough structures. For smoother surfaces, post-processing treatments might be needed, as in FDM for instance [43]. Alternatively, the LMH technique could be incorporated in laser-based systems, whereas the LMH function would be to construct the main underlying rough structure while the laser would provide the delicate details and the outer surface finish. This synergy may combine the advantages of the rough, low-cost LMH and the high-resolution laser-based techniques in more cost-effectively for the construction of relatively large objects. In this hybridization, the massive rough construction will be made by LMH and the fine details will be elaborated by the laser.

The preliminary results presented here call for additional studies in various directions, including the development of

advanced LMH applicators (also with magnetic coupling capabilities), and experimental and theoretical studies of various powders in different microwave frequencies. The raw material processed by LMH could be made of metals, ceramics or polymers, in either a powder or solid form. In particular, a wire feeding [24], instead of powder as in Fig. 1, may significantly improve the LMH resolution and also simplify the machine operation.

Higher frequencies and shorter wavelengths (e.g. in the millimeter range) may also improve the accuracy of localized sintering toward the sub-millimeter range. The operation in shorter pulses at higher power rates may also improve the spatial resolution as well as the energy efficiency. Further theoretical studies are also needed in order to incorporate micro-plasma and phase transition effects, as well as necking formation, into the coupled EM-thermal model of the LMH interaction with metal powders. In the stepwise construction level, further experimental studies are needed in order to examine new ways to construct 3D structures by LMH sintering (e.g. epoxy infiltration [49] may also be examined in LMH processing, as in DMLS).

In future systems, the energy transferred to the powder batch could be controlled more precisely by using feedback loops to monitor the temperature rise of the sample, and to adjust the microwave accordingly. The microwave system feeding the LMH applicator (Fig. 2b) may employ solid-state microwave generators (instead of magnetrons) to provide better controllability and compactness of the LMH system [38]. Though the LMH technology presented in this paper is yet premature, one may expect that its practical implementation in RP and AM systems would reduce the cost and size, and expedite the throughput of these systems.

Acknowledgement

This research was supported in part by the Israel Science Foundation under Grant No. 1639/11.

References

[1] Das S, Mukhopadhyay AK, Datta S, Basu D. Prospects of microwave processing: an overview. Bull Mater Sci 2009;32:1–13.
[2] Oghbaei M, Mirzaee O. Microwave versus conventional sintering: a review of fundamentals, advantages and applications. J Alloys Compd 2010;494:175–89.
[3] Rybakov KI, Olevsky EA, Krikun EV. Microwave sintering: fundamentals and modeling. J Am Ceram Soc 2013;96:1003–20.
[4] Roy R, Agrawal D, Cheng J. Full sintering of powdered-metal bodies in a microwave field. Nature 1999;399:668–70.
[5] Prabhu G, Chakraborty A, Sarma B. Microwave sintering of tungsten. Int J Refract Met Hard Mater 2009;27:545–8.
[6] Demirskyi D, Agrawal D, Ragulya A. Densification kinetics of powdered copper under single-mode and multimode microwave sintering. Mater Lett 2010;64:1433–6.
[7] Binner JGP, Caro R, Firkins J. Microwave sintering of nanometer and micrometer ferrite powders. J Microw Power Electromagn Energy 1999;34:131–6.
[8] Cheng J, Agrawal D, Zhang Y, Roy R. Microwave sintering of transparent alumina. Mater Lett 2002;56:587–92.
[9] Louzguine-Luzgin DV, Xie GQ, Li S, Inoue A, Yoshikawa N, Mashiko K, et al. Microwave-induced heating and sintering of metallic glasses. J Alloys Compd 2009;483:78–81.
[10] Gupta M, Wong WLE. Enhancing overall mechanical performance of metallic materials using two-directional microwave assisted rapid sintering. Scr Mater 2005;52:479–83.
[11] Leonelli C, Veronesi P, Denti L, Gatto A, Iuliano L. Microwave assisted sintering of green metal parts. J Mater Process Technol 2008;205:489–96.
[12] Gupta M, Wong WLE. Microwaves and metals. Wiley InterScience; 2007.
[13] Conner BP, Manogharan GP, Martof AN, Rodomsky LM, Rodomsky CM, Jordan DC, et al. Making sense of 3-D printing: creating a map of additive manufacturing products and services. Addit Manuf 2014;1–4:64–76.
[14] Levy GN, Schindel R, Kruth JP. Rapid manufacturing and rapid tooling with layer manufacturing (LM) technologies, state of the art and future perspectives. CIRP Ann Manuf Technol 2003;52:589–609.
[15] Li CH, Fang Z, Zhao HY. Investigation into layered manufacturing technologies for industrial applications. In: 2nd Int'l Conf. Multimedia and Information Technology. 2010. p. 213–6.
[16] Lin WS, Starr TL, Harris BT, Zandinejad A, Morton D. Additive manufacturing technology (direct metal laser sintering) as a novel approach to fabricate functionally graded titanium implants: preliminary investigation of fabrication parameters. Int J Oral Maxillofac Implants 2013;28:1490–5.
[17] Santos E, Shiomi M, Osakada K, Laoui T. Rapid manufacturing of metal components by laser forming. Int J Mach Tools Manuf 2006;46:1459–68.
[18] Agarwala M, Bourell D, Beaman J, Marcus H, Barlow J. Direct selective laser sintering of metals. Rapid Prototyping J 1995;1:26–36.
[19] Jain PK, Pandey PM, Rao PVM. Selective laser sintering of clay-reinforced polyamide. Polym Compos 2010;31:732–43.
[20] Droscher M, Schmidt FG. Method and device for producing three dimensional objects. United States patent US 6,243,616 B1; 2001.
[21] Chaim R, Levin M, Shlayer A, Estournes C. Sintering and densification of nanocrystalline ceramic oxide powders: a review. Adv Appl Ceram 2008;107:159–69.
[22] Twomey B, Breen A, Byrne G, Hynes A, Dowling DP. Rapid discharge sintering of nickel-diamond metal matrix composites. J Mater Process Technol 2011;211:1210–6.
[23] Planta X, Puliga F, Pallares A. Device and apparatus for selectively depositing molten plastic material and production method comprising selective deposition. European Patent EP 219195 (A1) 2010.
[24] Jerby E, Salzberg A, Meir Y, Planta X, Rubio R, Cavallini B. Method and devices for solid structure formation by localized microwaves. Int'l Patent Application PCT/IB2012/051425 2012.
[25] Jerby E, Meir Y, Salzberg A, Levy A, Rubio R, Planta X, et al. Stepwise consolidation of metal powder by localized microwaves for additive manufacturing of 3D structures. In: 14th Intl Conf microwave and high frequency heating. 2013. p. 345–8.
[26] Jerby E, Dikhtyar V, Aktushev O, Grosglick U. The microwave drill. Science 2002;298:587–9.
[27] Meir Y, Jerby E. The localized microwave-heating (LMH) paradigm – theory, experiments, and applications. In: GCMEA-2012 Proc. 2012. p. 131–45.
[28] Jerby E, Aktushev O, Dikhtyar V. Theoretical analysis of the microwave-drill near-field localized heating effect. J Appl Phys 2005;97, 034909-1-7.
[29] Cheng J, Liu C, Shang S, Liu D, Perrie W, Dearden G, et al. A review of ultrafast laser materials micromachining. Opt Laser Technol 2013;46:88–102.
[30] Jerby E, Aktushev O, Dikhtyar V, Livshits P, Anaton A, Yacoby T, et al. Microwave drill applications for concrete, glass and silicon. In: Conf Proc of the 4th world congress on microwave and radio-frequency applications. 2004. p. 156–65.
[31] Herskowits R, Livshits P, Stepanov S, Aktushev O, Ruschin S, Jerby E. Silicon heating by a microwave-drill applicator with optical thermometry. Semicond Sci Technol 2007;22:863–9.
[32] Livshits P, Dikhtyar V, Inberg A, Shahadi A, Jerby E. Local doping of silicon by a point-contact microwave applicator. Microelectron Eng 2011;88:2831–6.
[33] Jerby E, Dikhtyar V, Aktushev O. Microwave drill for ceramics. Am Ceram Soc Bull 2003;82:35–7.

[34] Jerby E, Thompson AM. Microwave drilling of ceramic thermal barrier coatings. J Am Ceram Soc 2004;87:308–10.
[35] Eshet Y, Mann R, Anaton A, Yacoby T, Gefen A, Jerby E. Microwave drilling of bones. IEEE Trans Biomed Eng 2006;53:1174–82.
[36] Jerby E, Golts A, Shamir Y, Wonde S, Mitchell JBA, LeGarrec JL, et al. Nanoparticle plasma ejected directly from solid copper by localized microwaves. Appl Phys Lett 2009;95:191501.
[37] Meir Y, Jerby E. Thermite-powder ignition by localized microwaves. Combust Flame 2012;159:2474–9.
[38] Meir Y, Jerby E. Localized rapid heating by low-power solid-state microwave-drill. IEEE Trans Microw Theory Tech 2012;60:2665–72.
[39] EOS, Electro Optical Systems, GmbH, Material data sheet, DirectMetal-20 for EOSINT M 270.
[40] Meir Y, Jerby E. Breakdown spectroscopy induced by localized microwaves for material identification. Microw Opt Technol Lett 2011;53:2281–3.
[41] Williamson JM, DeJoseph Jr CA. Determination of gas temperature in an open-air atmospheric pressure plasma torch from resolved plasma emission. J Appl Phys 2003;93:1893–8.
[42] Meir Y, Jerby E, Barkay Z, Ashkenazi D, Mitchell JB, Narayanan T, et al. Observations of ball-lightning-like plasmoids ejected from silicon by localized microwaves. Materials 2013;6:4011–30.
[43] Krolczyk G, Raos P, Legutko S. Experimental analysis of surface roughness and surface texture of machined and fused deposition modelled parts. Tehnički Vjesnik 2014;21:217–21.
[44] Meir Y, Jerby E. Magnetic fixation of metal powder for additive consolidation by localized microwaves [in preparation].
[45] Vandewalle N, Lumay G. Flow properties and heap shape of magnetic powders. AIP Conf Proc 2009;1145:135–8.
[46] Crangle J, Goodman GM. The magnetization of pure iron and nickel. Proc R Soc Lond A 1971;321:477–91.
[47] Pál G, Kun F, Varga I, Sohler D, Sun G. Attraction-driven aggregation of dipolar particles in an external magnetic field. Phys Rev E 2011;83, 061504-1-6.
[48] Coey JMD. Permanent magnet applications. J Magn Magn Mater 2002;248:441–56.
[49] Khaing MW, Fuh JYH, Lu L. Direct metal laser sintering for rapid tooling: processing and characterization of EOS parts. J Mater Process Technol 2001;113:269–72.
[50] Sustarsic B, Dolinesk S, Jenko M, Leskovšek V. Microstructure and mechanical characteristics of DMLS tool-inserts. Mater Manuf Processes 2009;24:837–41.
[51] Sereda PJ. Significance of microhardness of porous inorganic materials. Cem Concr Res 1972;2:717–29.
[52] Nikolic ZS, Wakai F. Three-dimensional computer study of rearrangement during liquid phase sintering Math. Comput Model 2012;55: 1251–62.
[53] Gu DD, Shen YF. Influence of phosphorus element on direct laser sintering of multicomponent Cu-based metal powder. Metall Mater Trans B 2006;37:967–77.
[54] Heigel JC, Michaleris P, Reutzel EW. Thermo-mechanical model development and validation of directed energy deposition additive manufacturing of Ti–6Al–4V. Addit Manuf 2014, http://dx.doi.org/10.1016/j.addma.2014.10.003 (in press).
[55] Martukanitz R, Michaleris P, Palmer T, DebRoy T, Liu Z-K, Otis R, et al. Toward an integrated computational system for describing the additive manufacturing process for metallic materials. Addit Manuf 2014, http://dx.doi.org/10.1016/j.addma.2014.09.002 (in press).
[56] Groza JR, Zavaliangos A. Sintering activation by external electrical field. Mater Sci Eng A 2000;287:171–7.
[57] Ma J, Diehl JF, Johnson EJ, Martin KR, Miskovsky NM, Smith CT, et al. Systematic study of microwave absorption, heating, and microstructure evolution of porous copper powder metal compacts. J Appl Phys 2007;101, 74906-1-8.
[58] Buchelnikov VD, Louzguine-Luzgin DV, Xie G, Li S, Yoshikawa N, Sato M, et al. Heating of metallic powders by microwaves: experiment and theory. J Appl Phys 2008;104:113505.
[59] Ignatenko M, Tanaka M. Effective permittivity and permeability of coated metal powders at microwave frequency. Physica B 2010;405: 352–8.
[60] Galek T, Porath K, Burkel E, Rienen U. Extraction of effective permittivity and permeability of metallic powders in the microwave range. Modell Simul Mater Sci Eng 2010;18:025015, 13pp.
[61] Rybakov KI, Semenov VE. Microwave heating of electrically conductive materials. Radiophys Quant Electron 2005;48:888–95.
[62] Roy R, Agrawal D, Cheng J. Experimental proof of major roll of magnetic field losses in microwave heating of metal and metallic composites. J Mater Sci Lett 2001;20:1561–3.
[63] Beloni E, Santhanam P, Dreizin E. Electrical conductivity of a metal powder struck by a spark. J Electrostat 2012;70:157–65.
[64] Yanagisawaa O, Kuramotoa H, Matsugia K, Komatsu M. Observation of particle behavior in copper powder compact during pulsed electric discharge. Mater Sci Eng A 2003;350:184–9.